Solid-State Encapsulation of Urea via Mechanochemistry-Driven Engineering of Metal–Phenolic Networks

Omid Mazaheri,[a,b,c] Ali Zavabeti,[b] Rebecca V. McQuillan,[b,c] Zhixing Lin,[b,c] Masood S. Alivand,[b,d] Enrico Della Gaspera,[e] Deli Chen,[a,c] Frank Caruso,[b,c] Helen Suter,[a,c]* and Kathryn A. Mumford[b,c]**

[a]School of Agriculture, Food and Ecosystem Sciences, Faculty of Science, The University of Melbourne, Parkville, Victoria 3010, Australia

[b]Department of Chemical Engineering, The University of Melbourne, Parkville, Victoria 3010, Australia

[c]ARC Hub for Smart Fertilisers, The University of Melbourne, Parkville, Victoria 3010, Australia

[d]Department of Chemical Engineering, Monash University, Clayton, Victoria 3800, Australia

[e]School of Science, RMIT University, Melbourne, Victoria 3001, Australia

*Corresponding authors. E-mail: fcaruso@unimelb.edu.au; helencs@unimelb.edu.au; mumfordk@unimelb.edu.au

ABSTRACT

Controlled-release fertilizers (CRFs) are sustainable alternatives as they can increase crop yield and minimize environmental contamination associated with conventional fertilizers. However, there remains a demand for the development of CRFs with high biocompatibility, and tunable morphologies and mechanical properties. Herein, a solvent-free mechanochemical method is developed for synthesizing urea-encapsulated metal–phenolic networks (urea–MPN matrices) as CRFs. The matrices exhibit tunable mechanical resistance, crystallinity, stiffness, and wettability properties via rearranging the internal structure of the MPNs and their subsequent interaction with the encapsulated urea crystals. Sample aging (7 days) leads to a higher degree of complexation of the MPNs, resulting in a material with increased elasticity and melting point relative to the as-synthesized sample. Thermal treatment (60 °C for 6 h) instigates structural reorganization of the urea crystals within the matrix, generating a more robust material with a 51-fold increase in Young's modulus. As CRFs, the urea–MPN matrices can be tuned to prolong the release of urea for up to 9 days depending on the treatment applied. As the mechanochemical synthesis of MPNs facilitates the tuning of physiochemical properties and has greater practicability for inclusion within large-scale processing, it has potential implementation within a broad range of industries.

INTRODUCTION

It is estimated that the global population will reach >10 billion people by 2050.[1,2] As a result, the increase in food demand imposes a pressing challenge for the agriculture sector and the environment, where fertilizers, particular urea as the dominant nitrogen fertilizer, play a pivotal role in increasing crop production.[1,3] However, the total utilization of urea by plants is reported to be as low as 30–45% owing to considerable loss to the environment through leaching and runoff, leading to the eutrophication of water bodies, and through gaseous ammonia and nitrous oxide emissions.[4,5] The poor efficiency of nitrogen use by plants is often due to the lack of synchronicity between nutrient supply and plant needs. Therefore, substantial efforts have been

directed toward developing controlled-release urea (CRU) to improve utilization and ease the environmental impact of urea while maximizing crop yield.[6–8] The main strategies that have been used to encapsulate urea for use as CRUs include spray coating of urea granules with a wide range of nonbiodegradable polymers (e.g., polysulfone, polyurethane, and polyolefins) and encapsulation of urea nanoparticles within a composite through mixing with biodegradable polymers (e.g., aliphatic polyesters and polysaccharides).[9–12] However, these strategies have limitations. For example, hydrophobic and impermeable polymers may cause soil contamination if they are not fully degraded and encapsulation typically involves a multistep procedure, leading to high production costs.[13,14] Moreover, encapsulation of urea using liquid mixing protocols requires the use of organic solvents at 40–130 °C and cross-linking agents, which complicates the process and presents challenges for large-scale production.[15–17] Therefore, the development of simple processes, which can also be upscaled, for producing CRUs is required.[2]

The application of mechanochemical approaches, wherein chemical reactions are induced by mechanical energy, has attracted widespread interest in sustainable production as they afford solvent-free, energy-saving, one-step procedures that are characterized by high production yields and low processing temperatures.[18] A wide range of organic molecules,[19] metal–organic frameworks,[20,21] supramolecular complexes,[22] alloys,[23] zeolites,[24–26] main-group elements,[27] polymers,[28] covalent organic frameworks,[29] nanoparticles,[30] and carbon materials[31,32] have been synthesized via mechanochemistry at both bench and industrial scales for use in various fields. Although the mechanosynthesis of urea ionic cocrystals and mechanochemical activation of layered minerals have been extensively studied for slow-release applications, synthesizing a biomass-based CRU via the mechanochemical approach needs further development—a comprehensive understanding of the intermolecular interactions between biomass and fertilizers would promote the rational design of tunable advanced CRUs.[33–38]

Biomass polyphenols, such as tannic acid (TA), are a group of compounds found in plants that can control the dissolution rate of urea in different types of media (i.e., soil and water environments) owing to the superior adhesion between polyphenols and urea conferred by hydrogen bonding, electrostatic interactions, and π–π stacking.[39,40] Moreover, this adhesion property facilitates the formation of biocompatible and scalable metal–phenolic networks (MPNs) through the chelation of catechol or galloyl groups of the phenolic ligands to metal ions on the urea surface.[41,42] The wide choice of applicable metal ions and phenolic ligands holds promise for an array of applications in the environmental, gas storage, biomedicine, and catalysis fields.[43] For instance, the investigation of MPNs as a controlled-release coating for urea granules has demonstrated how small environmental adjustments during MPN assembly influence MPN formation and growth on the urea granules, enabling tunable release profiles of urea.[44] Moreover, the use of mechanochemistry approach for the formation of MPN coatings on metal surfaces has been briefly investigated;[38] however, the underlying mechanism in enabling tunable engineering remains unexplored. Owing to the well-studied characteristics of MPNs and their demonstrated suitability to control the release of urea, the development of mechanochemically synthesized MPNs is desirable for integration into large-scale manufacturing streams.

Herein, we report the one-step, solvent-free mechanochemical synthesis for the assembly of MPNs in the presence of urea using the ball-milling technique. In this process, solid urea serves as a mediator for facilitating the coordination of the catechol groups of TA with metal ions (e.g., Ti^{IV}) in the solid state via the introduction of mechanical energy, resulting in a urea-encapsulated MPN matrix (i.e., urea–MPN matrix) (Scheme 1). The assembly of the MPNs leads to a decrease in the crystal size of urea and provides interfacial interactions (via noncovalent interactions including van der Waals forces, hydrogen bonding, and hydrophobic interactions), leading to the formation of a homogenous urea–MPN matrix. The bulk properties

(i.e., elasticity, melting point, and crystallinity degree) of the resulting urea–MPN matrix differ from those of pristine urea or TA owing to the formation of a hypoeutectic system. These differences are enhanced through aging and thermal treatments of the as-synthesized urea–MPN matrix that influence the binding strength, stability, and wettability of the MPNs. These treatments also influence the crystal lattice of urea and configuration structure of the MPNs, resulting in a change in the mechanical resistance, morphology, and porosity of the bulk urea–MPN matrix. Furthermore, the high oxidation state and formal charge of Ti^{IV} facilitates water trapping via the formation of a gel when the urea–MPN matrix is introduced in soil. The encapsulation of urea within the MPNs coupled with gelation formation that can occur in humid conditions make the urea–MPN matrices suitable as CRUs. The tunable and effective mechanochemical formation of such solid-state MPNs can potentially enable large-scale use within a broad range of industries.

Scheme 1. Schematic of the Mechanochemical Coordination-Driven Assembly of MPNs for Encapsulating Urea Crystals.[a]

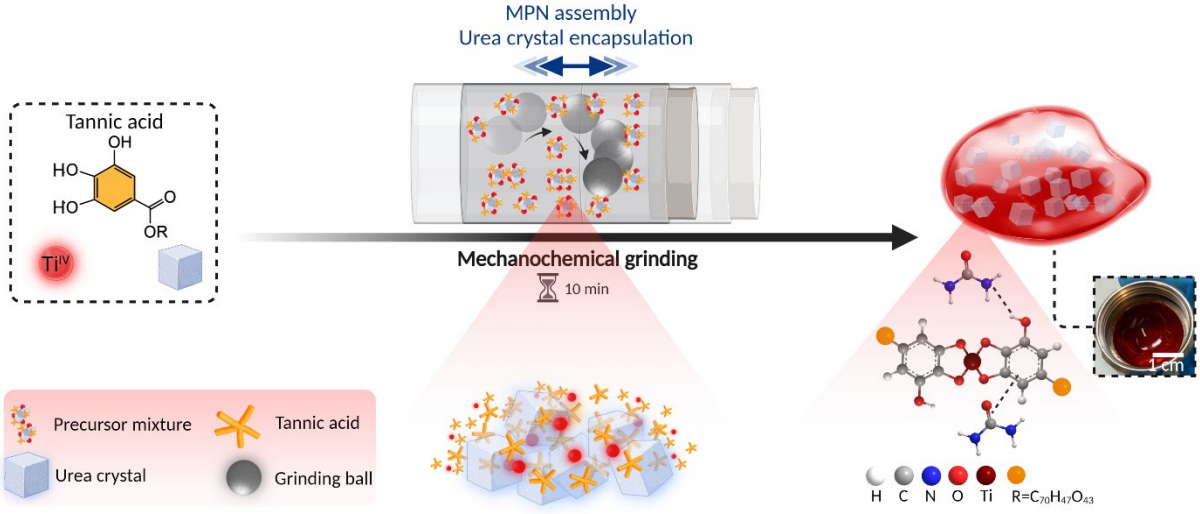

[a]The high friction conditions produced by mechanical grinding provide the required energy for Ti^{IV}–TA coordination in the solid state. The photograph shows the sample a few seconds after ball-milling.

EXPERIMENTAL SECTION

Materials. TA (ACS reagent), titanium(IV) isopropoxide ($Ti[OCH(CH_3)_2]_4$, 97%), iron(III) chloride hexahydrate ($FeCl_3 \cdot 6H_2O$, 99%), zinc(II) sulfate heptahydrate ($ZnSO_4 \cdot 7H_2O$, ACS reagent, 99.5%), zirconium(IV) chloride ($ZrCl_4$, ACS reagent, 99.5%), urea powder (ACS reagent, 99–100.5%), 4-(dimethylamino)benzaldehyde (*p*-DMAB, 99%), trichloroacetic acid (TCA, ACS reagent, 99%), hydrochloric acid (HCl, ACS reagent, 37%), and ethanol (98%) were purchased from Sigma-Aldrich. High-purity (Milli-Q) water with a resistivity of 18.2 MΩ cm was obtained from an inline Millipore RiOs/Origin water purification system. All solutions were freshly prepared for immediate use for each experiment.

Preparation of Urea–MPN Matrices. In a typical synthesis, TA (1.36 g), Ti^{IV} (0.24 g), and urea powder (2.4 g) were mixed for a few seconds using a glass spatula in a screw-capped stainless-steel jar along with a stainless steel ball bearing. The reaction vessel was then placed in a ball-mill machine, and components were ground with a frequency vibration setting of 25 Hz for 10 min. After grinding was complete, the urea–MPN sample was removed from the jar and subjected to different treatments: aging for 1 week (wrapped with polyethylene plastic and left on the bench at 25 °C) or heating at 60 °C for 6 h in an oven. The MPN content in the urea–MPN matrix was 40%. Unless specified otherwise, urea–MPN refers to matrices prepared with Ti^{IV}.

Preparation of Urea–MPN Matrices with Different MPN Contents. To prepare urea–MPN matrices with different MPN contents of 10, 20, and 40 wt%, respectively, TA (0.23, 0.53, or 1.36 g) and Ti^{IV} (0.04, 0.10, or 0.24 g) were mixed with urea (2.4 g) in a screw-capped stainless-steel jar along with a stainless steel ball bearing. The samples are denoted as urea–$MPN_{X\%}$, where X% is the wt% of MPN. Then, this reaction vessel was placed in a ball-mill machine, and components were ground with a frequency vibration setting of 25 Hz for 10 min. After grinding was complete, the urea–$MPN_{X\%}$ sample was removed from the jar and heated at 60 °C for 6 h in an oven.

Preparation of Urea–MPN Matrices with Different Metal Ions. To prepare urea–MPN matrices with different metals ions and an MPN content of 40%, TA (1.41, 1.38, 1.36, and 1.37 g) and Zr^{IV} (0.19 g), Fe^{III} (0.22 g), Ti^{IV} (0.24 g), and Zn^{II} (0.23 g) were respectively mixed with urea (2.4 g) in a screw-capped stainless-steel jar along with one stainless steel ball bearing. The samples were then ground using the same protocol as described above. The synthesized samples are referred to as urea–MPN_M, where M is the metal. After the grinding process was complete, the urea–MPN_M sample was removed from the jar and heated at 60 °C for 6 h in an oven.

Urea Release Studies. The urea release rates of the urea–MPN matrices were investigated in soil. The soil collected from the Wimmera region (Victoria, Australia) had the following characteristics: loamy sand, soil pH (1:5 H_2O) 8.4, total C 2.1%, NH_4^+-N 14 mg kg^{-1}, and NO_3^--N 19 mg kg^{-1}. The soil samples were first sieved (<2 mm particle size) to remove stones and air-dried to increase the homogeneity. After determining the water content of the soil samples via drying in an oven at 105 °C, the required amount of water was calculated to achieve a water-filled pore space (WFPS) of 60%. For each sample, soil (39 g) was placed in a 70 mL polypropylene container and preincubated for 3 days by hydrating the soil with the required water amount. After the preincubation period, the soil samples were treated by placing the urea–MPN samples on top of the soil with an application N rate of 840 mg kg^{-1} of soil. The treated soil samples were then incubated at either 10, 25, or 40 °C for 11 days. The soil moisture levels were kept constant by adding water based on weight loss every 3 days and samples were aerated at the same time. The urea–MPN matrices were sampled using a spatula at Day 1, 3, 5, 7, 9, and 11. After each sample collection, the urea–MPN samples were crushed and immersed in water (100 mL) for 3 h to dissolve the remaining urea. The solution was filtered to measure urea content using a colorimetric method. The urea content measurements were performed on the same day as when sample collection was performed to minimize the impact of urea

hydrolysis. The urea release experiments were conducted with three replicates. To investigate the influence of soil moisture on the release rate of urea from the urea–MPN matrices, the WFPS of the soil was set at 30, 40, or 60%, and the same procedure as described above was followed.

Water-Holding Capacity of Urea–MPN Matrices. The water absorbency of urea–MPN_{Ti} and urea–MPN_{Zr} matrices prepared with different MPN contents (10, 20, and 40%) was measured via changes in weight. The urea–MPN_{Ti} or urea–MPN_{Zr} matrix (1.0 g) was placed on a petri dish and stored in an incubator preset at 70% relative humidity (RH) at 25 °C. After 6 h, the sample was removed from the petri dish and weighed. The percentage absorbency was calculated using Equation S1:

$$\text{Absorbency } \% = \frac{w_2 - w_1}{w_1} \times 100\% \quad \text{(Equation S1)}$$

where w_1 is the weight of the dried sample and w_2 is the weight of the wet sample.

Water-Holding Capacity of Soil Treated with Urea–MPN Matrices. To investigate the water holding capacity of the soil when mixed with urea–MPN, dried soil (100 g) was thoroughly mixed with crushed urea–MPN samples at varying proportions (1, 2, and 3%) and the mixture was placed in a 4.5 cm diameter polyvinyl chloride tube with the base sealed with a 200 mesh nylon fabric and weighed (W_1). Then, the soil was slowly drenched with distilled water using a peristaltic pump (2 mL min^{-1}) to saturate the soil and weighed again (W_2). The water-holding capacity of the soil was calculated using Equation S2:

$$\text{Water-holding capacity } (\%) = \frac{W_2 - W_1}{W_1} \times 100\% \quad \text{(Equation S2)}$$

Water Retention of Soil Treated with Urea–MPN Matrices. To evaluate the water retention of soil when mixed with urea–MPN, soil (100 g) was mixed with urea–MPN sample (3 g) in a polypropylene container and weighed (W_0). Then, the mixture was drenched with distilled water to reach 60% WFPS moisture content in the soil and the container was weighed

(W_1). The container was incubated at room temperature and weighed every 2 days (W_i) for 14 days. The water retention of the soil was calculated as follows (Equation S3):

$$\text{Water retention (\%)} = \frac{W_i - W_0}{W_1 - W_0} \times 100\% \quad \text{(Equation S3)}$$

Urea Release Evaluated by Colorimetric Analysis. The concentration of urea was determined by UV–vis spectroscopy according to the methodology established by With et al. in 1961.[45] In brief, an Ehrlich reagent was prepared by dissolving *p*-DMAB (5 g) in HCl (37%) (20 mL) and diluting with ethanol in a 100 mL volumetric flask. To analyze the concentration of urea, the sample (0.5 mL; either standard or unknown urea concentration solutions) was mixed with Ehrlich reagent (0.5 mL) in a cuvette. Then, TCA (10% in water, 2 mL) was added to the cuvette. *Caution! TCA is corrosive and toxic to some organs and should be handled carefully.* A curve of urea concentration (30–1000 ppm) in solution versus absorbance at λ = 420 nm was obtained with $R^2 = 0.9997$.

Material Characterization. UV–Vis diffuse reflectance spectroscopy (UV–Vis DRS) was performed on an Agilent Cary 5000 spectrophotometer equipped with an integrating sphere. A center-mount attachment equipped with a custom-made powder holder was used, enabling the positioning of the samples within the integrating sphere. This measures reflectance/scattering losses and therefore the pure absorptive component of the prepared materials can be obtained.

X-ray photoelectron spectroscopy (XPS) data were obtained on a VG ESCALAB 220i-XL spectrometer equipped with a hemispherical analyzer. Monochromatic Al Kα X-ray (1486.6 eV) at 220 W (22 mA and 10 kV) was used as incident radiation. Pass energies were set at 100 and 50 eV for the survey (wide) and high-resolution scans, respectively. Survey scans were accomplished at 1 eV step size and 10 ms dwell time, whereas high-resolution scans were obtained over a 20 eV binding energy range with a 0.05 eV step size and 100 ms dwell time. The base pressure in the analysis chamber was set to $<8.0 \times 10^{-9}$ mbar and a low energy flood gun was used to compensate for surface charging effects. CasaXPS software was used to

process the data, and calibration was performed based on the C 1s peak reference at 285.0 eV for energy calibration.

Raman spectroscopy analysis was performed on a Renishaw system (inVia Qontor) equipped with a Peltier-cooled CCD detector and coupled to an Olympus BH-2 confocal microscope. A near-infrared diode laser with a wavelength of 532 nm was used as the excitation source. Laser power at the sample was set to 0.01 mW with 1 s step time and 10 min dwell time. The spectra were recorded over a range of 500–1800 cm^{-1} with a spectral resolution of 1 cm^{-1} using a 50× microscope objective. For sample preparation, the samples were placed on a quartz microscope slide. The collected raw spectra were smoothed using a Savitzky–Golay smoothing filter.

Scanning electron microscopy (SEM; (Hitachi FlexSEM 1000) was used to study the morphology of the urea–MPN samples. A secondary electron detector and an accelerating voltage of 20 kV were used. The surface of the samples was coated with 10-nm gold using an ionization chamber sputter coater (Quorum K575X) before SEM imaging. For each specimen prepared, three samples were randomly chosen for imaging.

Attenuated total reflectance Fourier transform infrared (ATR-FTIR) spectroscopy was performed on a Bruker TENSOR II system in the range of 400–4000 cm^{-1}; a total of 64 scans were measured per run.

X-ray diffraction (XRD) analysis was conducted on a Bruker D8 Advance X-ray diffractometer equipped with Ni-filtered Cu Kα radiation (1.54 Å, 40 mA, and 40 kV); a step size of 0.02 was used.

Compression tests were performed to evaluate the mechanical properties of the samples using a 2 kN load cell on an Instron 5848 Microtester (Norwood, MA, USA). Compression was performed at 0.0166 mm s^{-1}. Recordings started after 0.01 N preload was exceeded.

Differential Scanning Calorimetry (DSC) analysis was carried out on a PerkinElmer Pyris-1 DSC instrument. The samples were first heated from 20 to 150 °C at a heating rate of 20 °C

min^{-1}, then cooled to 20 °C at a cooling rate of 20 °C min^{-1}, and finally heated a second time from 20 to 150 °C at a heating rate of 20 °C min^{-1}, then cooled to 20 °C at a cooling rate of 20 °C min^{-1}.

Thermogravimetric analysis (TGA) was performed using a NETZSCH TG 209 F1 Libra analyzer and coupled to a Fourier transform infrared module (ALPHA, Bruker). The samples were heated in the range of 50–600 °C at a heating rate of 10 °C min^{-1} under an O_2/N_2 (80/20 %) stream at a gas flow rate of 20 mL min^{-1}.

The water contact angles (WCAs) of the samples were determined using a Theta optical tensiometer (ATA Scientific, Australia) and a droplet of distilled water at room temperature.

Micro-computed tomography (micro-CT) scanning was performed with a Phoenix Nanotom M nano-CT 3D scanner (Waygate Technologies) running on the xs control and Phoenix datos|x acquisition software (Waygate Technologies). The samples were placed in 2-mL plastic vials for micro-CT scanning and brought in close proximity to the X-ray source. The samples obtained after aging and heating treatments were scanned at a resolution of 7.0 μm using an energy of 60 kV. A current of 300 μA and a tungsten target were used to run the instrument in fast-scan mode. A total of 1200 X-ray projections were collected through a 360° rotation of the samples over the course of a 10 min scan (no averaging or skipped images and an integration time of 500 ms). Volume reconstruction of the micro-CT data was carried out using Phoenix datos|x reconstruction software, and applying a median filter and a region of interest filter during reconstruction. The data were exported as 16-bit volume files for analysis using the Avizo (Thermo Fisher Scientific) software suite. Samples were segmented using the interactive threshold tool of Avizo to create a binary image of urea–MPN (intermediate gray phase), and pore space within the sample (dark gray to black phase). The volume fraction of each phase was then determined by comparing the binary images of each phase to a sample mask using the Volume Fraction tool in Avizo.

Transmission electron microscopy (TEM) and energy-dispersive X-ray spectroscopy (EDX) mapping were performed on a JEOL 2100F microscope equipped with an Oxford X-Maxn 5 80T EDX detector Gatan OneView 4k camera. An acceleration voltage of 200 kV was used for imaging and mapping. Prior to analysis, the samples were first dispersed in acetonitrile (0.05 wt% solution), then a single droplet was dropped onto a formvar carbon-coated copper TEM grid and then dried overnight at room temperature in a vacuumed desiccator. The concentration of urea in the soil studies was determined on an Agilent Cary 300 UV–vis spectrophotometer equipped with a diode array detector.

The general instrumentation used is as follows. Mass measurements were performed using a highly accurate (±10 μg) analytical balance (Mettler Toledo XS205). A high-speed vibration machine (TissueLyser II, 300 W motor power) was used for grinding. The samples were placed in a 4.5 cm (diameter) by 5.5 cm (height) screw-capped stainless-steel jar along with one stainless steel ball bearing (1.5 cm diameter). An incubator (Thermoline Scientific, TLM-590) was used for the soil studies. The Smart Mist Top™ Connect Humidifier (Breville, Australia) was used for adjusting the RH of the incubator. RH values of the incubator were remotely monitored via humidity gauge (ThermoPro 260FT with ± 2% RH accuracy). A peristaltic pump (Gilson, Miniplus evolution) was used for the water-holding capacity studies.

The software used is as follows. TEM image analysis was carried out using the Gatan Microscopy Suite 1.8.4. software. The *d*-space lattices of urea crystals from Gatan were identified and matched with the database using the Vesta software (V. 3.5.7). ChemDraw and Chem3D software (v. 21.0.0) were used to draw the molecular structure of components. Schematic illustrations were created using the Biorender online platform and the open access Blender software.

RESULTS AND DISCUSSION

Mechanochemical Synthesis of Urea–MPN Matrix. A mechanochemistry approach was examined for the formation of MPNs under high friction conditions, where Ti^{IV} was chosen as the metal and TA, which is inexpensive and environmentally friendly was selected as the polyphenol (Scheme 1). From our preliminary evaluation, stable bis or tris Ti^{IV}–TA complexes were not obtained, indicating that a basic compound is required to form stable Ti^{IV}–TA complexes in the solid state. To evaluate this, urea, a mild alkaline compound, was used to mediate the complexation of Ti^{IV}–TA via the deprotonation of the catechol groups of TA (Figure 1a). To understand the role of urea, the chemical interactions that occur during MPN assembly were assessed.

UV–vis DRS analyses of pure TA, urea, Ti^{IV}–TA, and urea–MPN matrix revealed considerable differences in their absorbance patterns (Figure 1b). Ti^{IV}–TA complexes obtained upon mechanical grinding in the absence of urea featured a weak ligand-to-metal charge-transfer (LMCT) absorption band within the range of ≈450–700 nm, with a λ_{max} of 570 nm, confirming the formation of Ti^{IV}–TA mono/bis-complexes.[46] However, the resulting Ti^{IV}–TA complexes dissolved after immersion in water, confirming the need for an alkaline component to form stable MPNs in solid state. The formation of MPNs in the presence of urea (urea–MPN matrix) was confirmed by both an increase in the intensity of the absorbance peak and a shift to lower values within the range of 380–600 nm, indicative of stable bis and tris Ti^{IV}–TA complexes even after immersing the sample in water.[47]

The formation of MPNs was further assessed by performing high-resolution XPS on the control samples (i.e., TA and Ti^{IV}–TA) and urea–MPN matrix (Figure 1c,d). The XPS pattern of Ti^{IV}–TA featured Ti $2p_{3/2}$ and Ti $2p_{1/2}$ signals at 458.4 and 463.8 eV, respectively, which shifted to slightly higher energies of 458.6 and 464.1 eV in the XPS pattern of urea–MPN matrix.[48] The spin-orbit splitting of Ti $2p_{3/2}$ and Ti $2p_{1/2}$ is ~5 eV in both samples and could be assigned to the Ti^{IV}–O bonds in the Ti^{IV}–TA complexes.[47] In addition, the core-level O 1s XPS

pattern of urea–MPN matrix featured peaks at 531.7 and 533.2 eV, which are characteristics of C=O and C–O/O–C–O bonds, respectively. These peaks shifted to lower energies relative to those of TA and Ti^{IV}–TA, indicative of coordination interactions between Ti^{IV} and TA.[49,50]

To further examine the coordination structure of the urea–MPN matrix, Raman analysis was conducted on the urea–MPN matrix and compared to the control samples (urea–TA and Ti^{IV}–TA) (Figure 1e). The Raman spectrum of urea–TA displayed strong bands at 1612 and 1716 cm^{-1}, which were attributed to the stretching vibration of the benzene ring and C=O stretching modes. The intensity of those bands decreased considerably upon interactions of TA with Ti^{IV} in Ti^{IV}–TA and urea–MPN matrix.[51] The band at 1716 cm^{-1} was nearly absent from the spectra of Ti^{IV}–TA and urea–MPN matrix, whereas the band at 1711 cm^{-1} broadened and shifted to a lower wavelength as a result of complexation with Ti^{IV}. Furthermore, the spectra of Ti^{IV}–TA and urea–MPN matrix displayed three new bands at 630, 1360 (υ_1), and 1495 (υ_2) cm^{-1}, which were attributed to the molecular reorganization of TA upon coordination of the galloyl and carboxylate groups with Ti^{IV}, respectively. The difference in the Raman shift of these two bands ($\Delta\upsilon = \upsilon_2 - \upsilon_1$) decreased from 136 to 132 cm^{-1} after the addition of urea, suggesting that the structure of some of the carboxylate ester (–COOR)–Ti^{IV} interactions changed from bidentate bridging to chelating mode (Figure 1a).[52] Moreover, the intensity ratio of υ_2/υ_1 increased from 1.00 for Ti^{IV}–TA to 1.19 for urea–MPN matrix ; these observations confirm that metal–phenolic coordination is heavily influenced by the pK_a of the precursors through the solid-state grinding process, where the ionization of phenol to phenolate groups induces a negative mesomeric effect through transferring pi-bond electrons from the conjugate system of the benzene rings to $–COO^-Na^+$ groups. Thus, the electron density of the conjugate system is reduced, which increases the bond order of the C=C bonds in the aromatic ring, and leads to a more intense υ_2 band.[51] Our findings reveal that the binding strength of the Ti^{IV}–TA complexes enhances, thereby improving the stability of the urea–MPN matrix. SEM analyses of TA,

ground urea, and urea–MPN matrix indicated that both TA and urea crystals underwent shape restructuring after coordination with Ti^{IV} metal ions during MPN assembly (Figure 1f–h). A few small urea crystals were observed in the urea–MPN matrix but they were smaller than the ground urea crystals (Figure 1g,h). The presence of Ti^{IV}–TA possibly further facilitates the breakdown and encapsulation of urea crystals within the MPNs via noncovalent interactions (e.g., van der Waals forces, hydrogen bonding, ionic bonding, and π–π stacking) and strong surface coordination and assembly (Figure 1a).[53] For example, it is reported that the binding of urea with polyphenols under mechanochemical conditions is predominantly through hydrogen binding, where $–NH_2$ of the amide binds to deprotonated catechol groups. Also, the formation of such an intermediate Ti^{IV}–NH_2–TA complex is likely,[33,54–56] in which urea can act as a catalyst to facilitate the formation of MPNs under solvent-free conditions. Furthermore, the temperature of the internal jar wall was ~42 °C (recorded by an infrared thermometer gun). This localized heat can enhance the coordination between Ti^{IV} and TA, as well as intensify the interactions between urea crystals and MPNs. It is noted that this local temperature can be influenced by the milling frequency and the number and size of balls in the jar.[57,58] Additionally, EDX mapping of a high-angle annular dark-field (HAADF) image of a representative area of the urea–MPN matrix confirmed the homogeneity of the MPNs, with uniform distribution of Ti, N, and C throughout the structure (Figure 1i). Therefore, these findings reveal that Ti^{IV}–TA imparts properties to the urea–MPN matrix, including intercalated small urea crystals, that enable control over the release profile of urea, as discussed in *Urea–MPN Matrices as CRUs*.

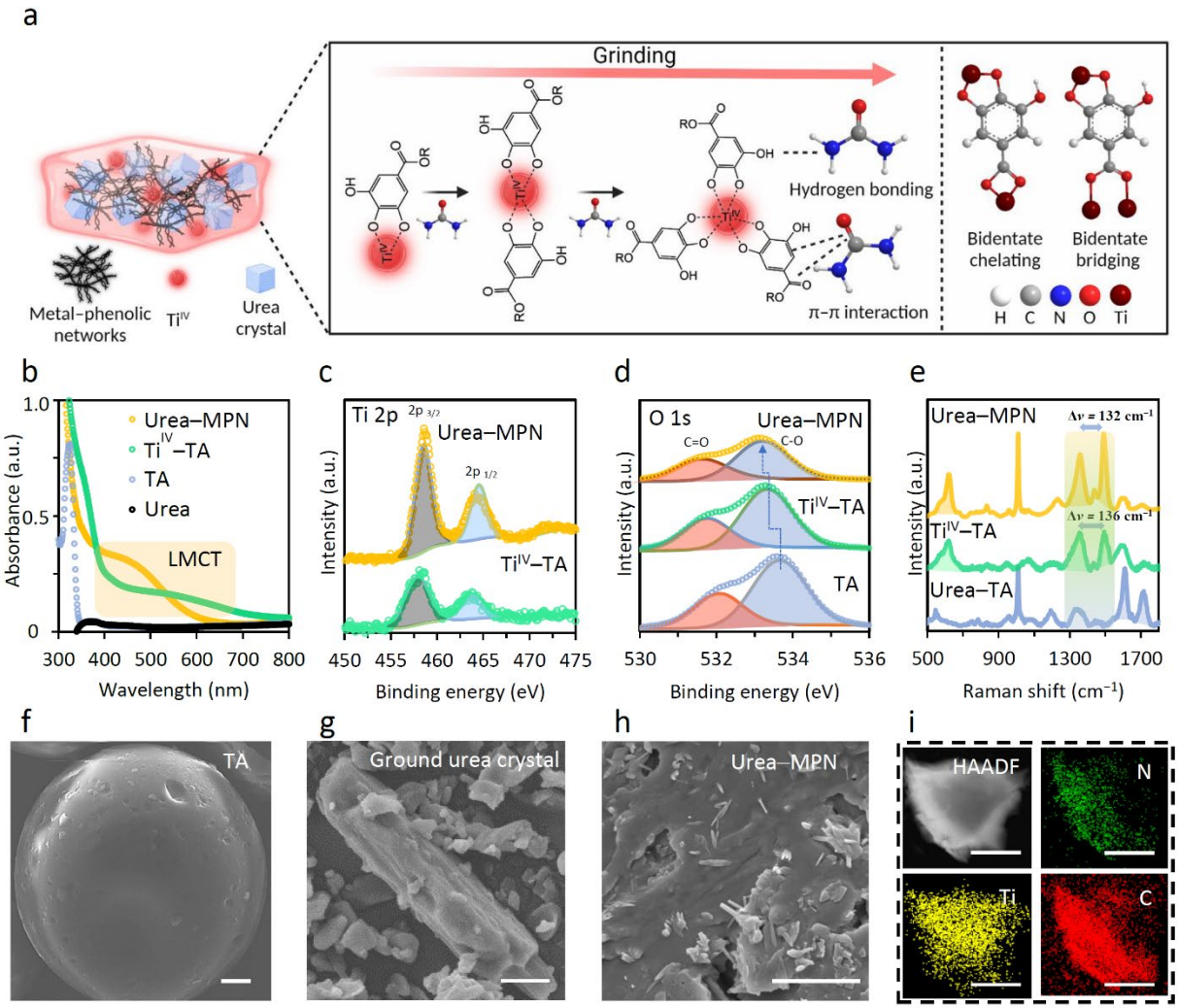

Figure 1. Urea-mediated coordination-driven assembly of MPNs via grinding. (a) Schematic of the assembled urea–MPN matrix via grinding and possible complexation states of Ti^{IV}–TA. (b) UV–Vis DRS spectra of urea, TA, Ti^{IV}–TA, and urea–MPN matrix; the highlighted area (400–700 nm) corresponds to the LMCT band of the Ti^{IV}–TA complexes. (c) Ti 2p XPS patterns of the Ti^{IV}–TA complexes and urea–MPN matrix. (d) O 1s XPS patterns of TA, Ti^{IV}–TA complexes, and urea–MPN matrix. (e) Raman spectra of urea–TA, Ti^{IV}–TA complexes, and urea–MPN matrix. (f–h) SEM images of the surfaces of TA, ground urea, and urea–MPN matrix. Scale bars are 10 μm. (i) HAADF and EDX mapping images of urea–MPN matrix. Scale bars are 5 μm.

Aging and Thermal Treatment of Urea–MPN Matrix. A fundamental understanding of age- and heat-induced structural reorganization of MPNs could offer opportunities to rationally fine-tune the properties of materials and their overall performance in specific applications. Therefore, the effects of aging and heat treatments on the fabricated urea–MPN matrix were investigated. Samples were either aged for 1 week at 23 °C or heated at 60 °C for 6 h (*aged* and *heated* samples, respectively). Both treatments were compared with the as-synthesized urea–MPN matrices, promptly after preparation (*fresh* sample).

From the UV–vis DRS results shown in Figure 2a, both aging and heating induced structural changes in the MPNs. Aging led to an increase in the absorbance of the metal–phenolic complexes without a shift in the LMCT band, indicating the similar complexation state of Ti^{IV}–TA present in the aged and fresh samples. In contrast, heating resulted in an increase in the extent of coordination and transition of the dominant Ti^{IV}–TA complexation state from bis to tris-complexes. In addition, comparison of the XPS results of the fresh sample and the aged and heated samples (Figure 2b) revealed the shift of the N 1s core-level peak (400.1 eV), representative of the $–NH_2$ group of urea, to lower energies (399.9 and 399.7 eV, in the aged and heated samples, respectively). This decrease in binding energy likely represents an increase in the strength of interactions of urea with MPNs via hydrogen bonding.[44,56] Moreover, the XPS patterns of the C 1s core-level peaks showed that the C=O and C–O peaks underwent structural reorganization during sample aging and heating, as observed from the shift of the binding energies of 289.8 and 286.4 eV to a lower energy (by ≈0.9 eV) after heating (Figure 2c). This observation is consistent with the Raman spectroscopy analyses of the Ti^{IV}–TA, fresh, aged, and heated samples, which showed an increase in the υ_2/υ_1 ratio from 1 (Ti^{IV}–TA) to 1.31 (heated sample), leading to a decrease in $\Delta\upsilon$ from 136 to 125 cm^{-1} (Figure 2d). These observations likely suggest a higher level of deprotonation of the catechol/galloyl groups and a higher extent of bidentate Ti^{IV}–COO bridging mode involved in the samples through

structural rearrangement after aging or heat treatment.[51] The broad peak at ≈3300 cm^{-1} in the FTIR spectra of urea–TA, fresh, aged, and heated samples was assigned to the –OH and –COOR groups of TA; the intensity of the peak decreased in the order of urea–TA > fresh > aged > heated (Figure 2e); the incorporation of the –OH and –COOR functional groups of TA toward the formation of the TA–Ti^{IV} coordination complex can lead to a decrease in the peak intensity.[59]

The degree of crystallinity within the urea–MPN matrices increased upon aging and heat treatments, while the crystal lattice of urea remained intact upon grinding (Figure 2f and Figure S1).[60,61] Although this increase is likely due to the partial oxidation of TA, which alters the growth of the MPNs, the mechanism is unclear as the crystallinity of urea also needs to be accounted for. Moreover, the formation of by-product biuret was ruled out as investigated by XRD analysis of urea–MPN matrices following the grinding; the heat generated (<150 °C) during ball-milling is likely insufficient to result in biuret formation.[62]

Overall, these results indicate that the physiochemical properties of the urea–MPN matrix are age- and temperature-dependent, displaying age- and heat-induced structural rearrangement.

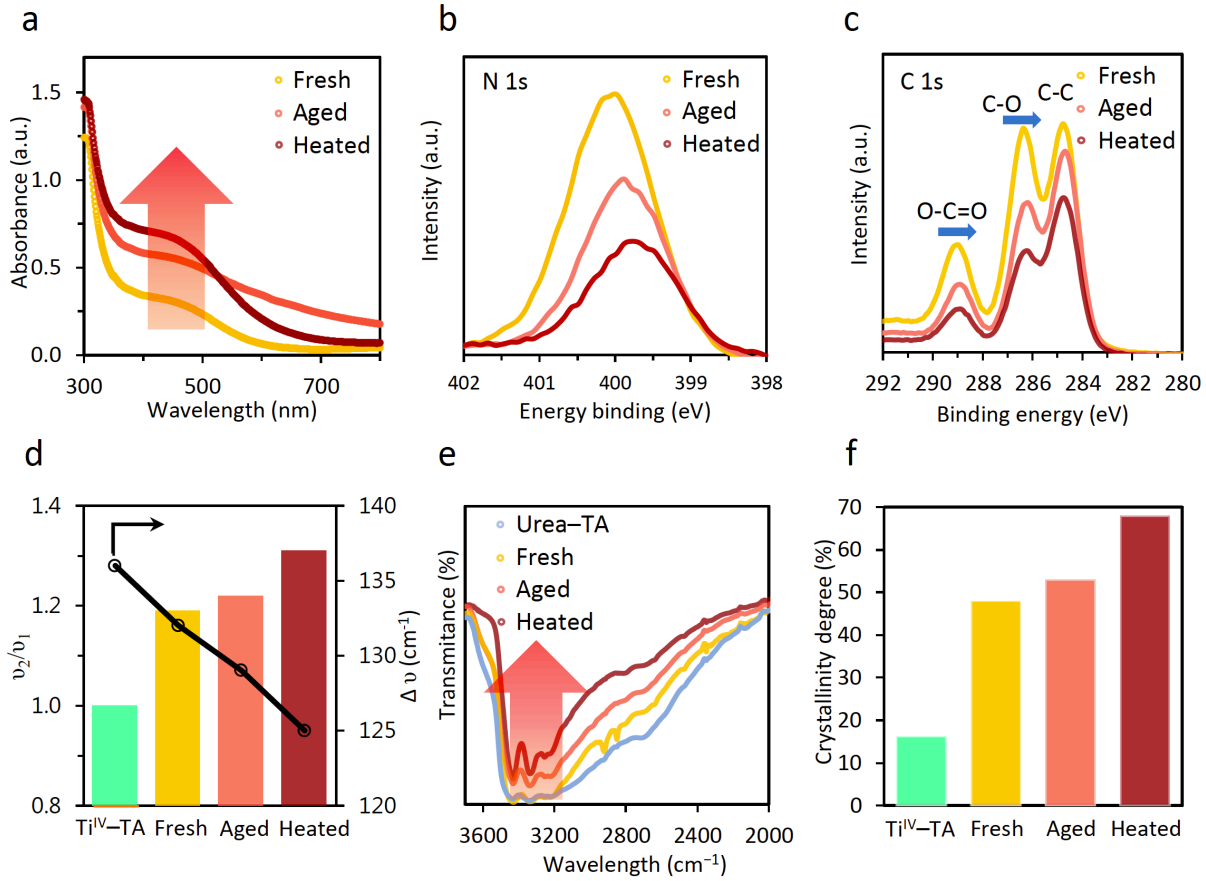

Figure 2. Influence of aging (1 week at 23 °C) and thermal treatment (60 °C for 6 h) on the physicochemical properties of urea–MPN matrix. (a) UV–Vis DRS spectra and (b,c) high-resolution N 1s and C 1s XPS patterns of fresh, aged, and heated urea–MPN matrices. (d) υ_2/υ_1 ratio profiles (bar graph) and $\Delta\upsilon$ (black line) of Ti^{IV}–TA, and fresh, aged, and heated urea–MPN matrices measured by Raman spectroscopy. (e) FTIR spectra of urea–TA, and fresh, aged, and heated urea–MPN matrices. (f) Degree of crystallinity of Ti^{IV}–TA, and fresh, aged, and heated urea–MPN matrices, as measured by XRD in the range of $2\theta = 5–50°$.

Structural and Lattice Properties of Urea–MPN after Aging and Heat Treatments. To gain further insight in the underlying mechanism of the age- and heat-induced structural reorganization of the encapsulated urea in MPNs, we examined the nanoscale structure of the samples. SEM revealed the smoother surface of the urea–MPN matrix following heating relative to that of the aged urea–MPN matrix (Figure 3a,b). During heat treatment, it is likely

that the small individual urea crystals coalesce into a single larger entity within the MPNs, resulting in a uniform matrix. During aging, small individual urea crystals are still observed within the MPNs, which results in a rough surface morphology (Figure 3a,c).

To elucidate the crystallographic properties of the matrices after aging and heating, TEM was performed. Figure 3d,h shows low-magnification images of the aged and heated urea–MPN matrices, respectively; both aging and heating reduced the crystal size of urea. Selected area electron diffraction (SAED) analysis confirmed the crystallinity of the samples (Figure 3e,i): the aged sample showed at least six diffraction rings, corresponding to the crystal planes i.e., (211), (002), (311), (222), (203), and (411) of urea and indicative of a poorly crystalline structure.[63] In contrast, heating changed the crystallinity state from a poorly crystalline with small grain sizes to a highly crystalline structure with larger domains, as depicted from the distinct bright reflections associated with 001, 101, 110, and 200 indices, which are related to the tetragonal lattice with $P42_1m$ space group of urea (Figure 3i).[64] High-resolution TEM (HRTEM) was used to further investigate the crystalline properties of the samples (Figure 3f,j and Figure S2). Several small grain boundaries with varying orientations (assigned in random colors) were observed in the aged sample, which were embedded in an amorphous MPN matrix, confirming the hypothesis that small crystalline grains are present within the aged sample. In contrast, the heated sample was highly crystalline with larger crystal domains. Regardless of the degree of crystallinity of the samples, HAADF and elemental mapping revealed a homogeneous distribution of urea and MPN elements (i.e., C, N, and Ti) in both the aged and heated samples, indicating the successful encapsulation of urea crystals within the MPNs (Figure 3g,k).

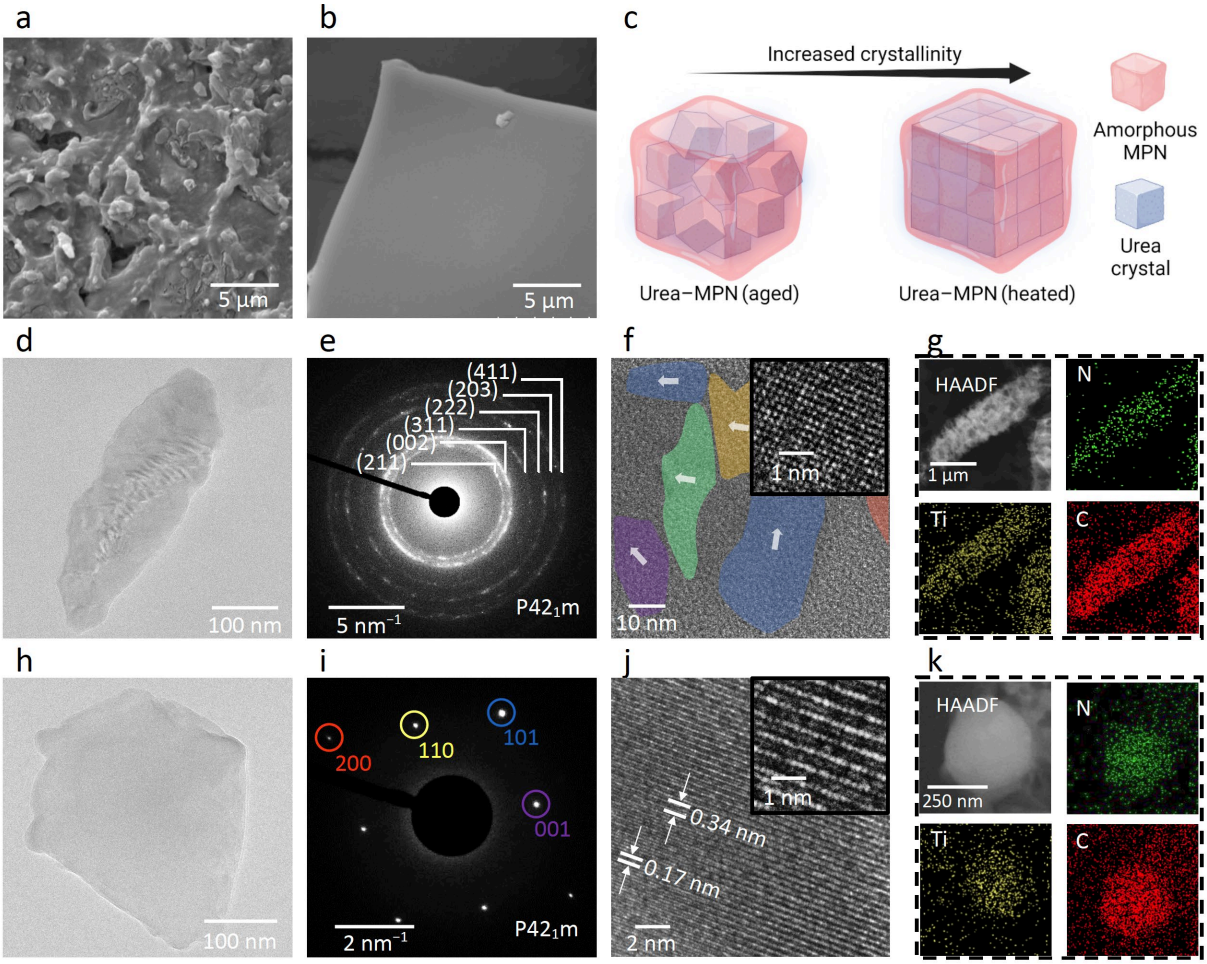

Figure 3. Structure modulation of urea crystals in urea–MPN matrix via aging and thermal treatments. (a,b) SEM images of the surface of urea–MPN matrix after aging (a) and heating (b). (c) Schematic of structure reorganization of urea crystals in the urea–MPN matrix after aging and heat treatments. (d,h) TEM, (e,i) SAED, (f,j) HRTEM, and (g,k) HAADF–mapping images of urea–MPN matrix after aging (d–g) and heat (h–k) treatments. Insets in (f) and (j) show the lattice spacing in urea crystals.

Bulk Properties of Urea–MPN Matrix Following Aging and Thermal Treatments. To further understand the influence of aging and heat treatments on the physical properties of urea–MPN matrix, the mechanical and thermodynamic behavior of the urea–MPN matrix were examined. A comparative analysis of the mechanical resistance of urea, and fresh, aged, and heated urea–MPN matrices was conducted via a diametral compression test (Figure 4a).

Relative to urea, which displayed a low compression strength of 127 Pa, all three urea–MPN matrices displayed significantly greater mechanical resistance. This observation highlights the major role of hydrogen bonding, ionic bonding, and π–π stacking within the samples (Figure 1a), where increased molecular interactions between the encapsulated urea and MPNs and oxidation-based cross-linking of TA can provide additional mechanical strength.[65,66] Furthermore, both the fresh and aged samples showed high malleability, avoiding rupturing even after ≈75% deformation was reached. The pliability of these matrices may be attributed to the branched structure of TA and the overall lattice structure of urea within the fabricated MPNs. The strain required for the deformation of the aged sample in the elastic region, which corresponds to crystal deformation, markedly increased compared with that required for the fresh sample. A significant compression strength (≈400 Pa) was observed after heating the urea–MPN matrix in contrast to the plasticity observed for the fresh and aged samples. Hence, we propose that an intermolecular rearrangement between the galloyl groups of TA and Ti^{IV}–TA building blocks leads to defects in the urea–MPN matrix.[67] At a molecular level, this may suggest that the MPNs become more compact with cooling,[67] leading to urea crystals adjoining into larger crystal lattices. Furthermore, the energy required for the deformation of 1 g sample was evaluated and enables comparison of the mechanical resistance of different samples. The normalized energy was achieved by integrating load–deformation plots up to a deformation point of 25% and dividing by the sample mass to ensure direct comparison (Figure 4b).[68] Relative to the fresh sample, both the aged and heated samples required more energy for compression. This different energy requirement is possibly because of the different content of the urea crystal lattice; the content increased in the order of fresh < aged < heated samples. The energy required for the deformation of a highly crystalline structure is typically higher than that required for a poorly crystalline material with smaller crystal lattices. The Young's modulus (E_Y), a measure of stiffness, of the urea–MPN matrices before and after aging and

heat treatments was determined from the slope of the compression curves in their elastic regions (Figure 4c). The fresh urea–MPN matrix showed a lower stiffness, having an E_Y of 0.1 MPa, than the aged and heated urea–MPN matrices, whose stiffness increased by ≈7 and 51 fold, respectively. The increase in stiffness displayed by the treated urea–MPN matrices is ascribed to changes in the crystallinity of urea within the matrices and the increased degree of complexation of the Ti^{IV}–TA complexes.

To better understand the relationship between sample stiffness and crystallinity, DSC and TGA were conducted. The DSC curves of the urea–MPN matrices all showed an endothermic peak at lower temperatures of 92–114 °C when compared with that of pure urea observed at 135 °C (which is attributed to its melting point)[69] (Figure 4d). The homogeneity of the urea–MPN matrices results in the formation of a hypoeutectic system, which displays an overall lower melting point than that of each individual constituent of the matrix (Figure S3). For example, the melting point of the urea–MPN matrix increased from 92 °C (fresh sample) to 100 and 114 °C, after aging and heating, respectively. The higher melting point observed for the heated matrix, aside from a change in the stiffness, potentially indicates the formation of a larger urea crystal within the MPN matrix.[16] From the TGA results, an improvement in the thermal stability of the samples was observed suggesting that more energy was required for dissociation of the urea crystals and Ti^{IV}–TA complexes in the aged and heated samples compared with that required for the fresh sample (Figure 4e).

The increasing hydrophobicity of the aged and heated samples, relative to the fresh sample, was assessed through surface wettability measurements. The aged and heated samples had larger WCAs of 60 and 68°, respectively, than the fresh sample (45°) (Figure S4), which is likely due to the structural rearrangement of the Ti^{IV}–TA complexes driven by an increase in π–π stacking among the aromatic rings in TA (Figure 4f).[67]

The urea–MPN matrix expanded upon heat treatment when compared to the aged sample. Thus, X-ray micro-CT was performed to better evaluate the bulk arrangement within the material matrix; both cross-sectional and computed void volume images were analyzed (Figure 4g–i). The heated sample showed higher porosity than the aged sample, thus confirming the expansion observed upon heating (Figure 4g,h insets and Movies S1 and S2). This finding may indicate an important relationship between urea crystal rearrangement and phase change behavior within MPN structures, thus further fundamental studies on the solid-state formation of MPNs at different temperatures are needed.

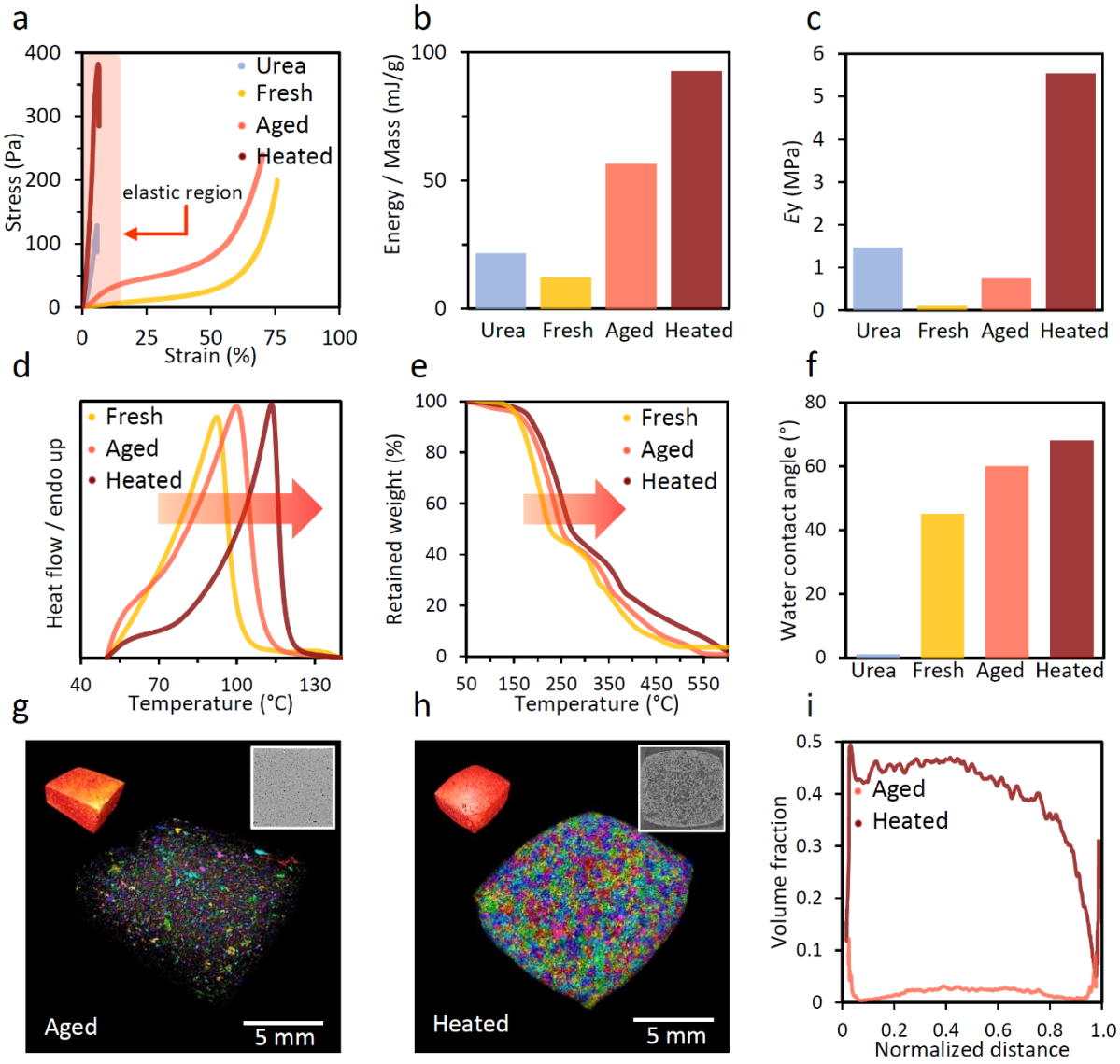

Figure 4. Influence of aging and thermal treatments on the mechanical and bulk properties of urea–MPN matrices. (a) Compressive stress–strain curves, (b) calculated energy required to reach 25% deformation, and (c) corresponding Young's modulus values derived from elastic regions of compression studies performed on urea, fresh, aged, and heated samples. (d) DSC and (e) TGA curves of the fresh, aged, and heated urea–MPN matrices. (f) WCAs of urea, fresh, aged, and heated samples. (g,h) Micro-CT images of urea–MPN matrices after aging (g) and heating (h); insets show the corresponding cross-sectional images. The porosity of the samples in the micro-CT images is displayed with randomized colors. (i) Volume

reconstruction of the micro-CT data of the aged and heated samples from ≈1200 scan projections.

Urea–MPN Matrices as CRUs. The cumulative release profile of urea from the urea–MPN matrices in soil was evaluated and compared against that of pure urea; the experimental set-up is shown in Figure 5a. A colorimetric method was used to calculate the dissolution of urea from the urea–MPN matrix as a function of time. The WFPS percentage (representative of the water content of soil) and environmental temperature of the soil were kept constant at 60% and 25 °C, respectively, in all experiments unless otherwise mentioned.

The different urea–MPN matrices (fresh, aged, and heated) all showed a prolonged urea release profile in comparison to pure urea—urea release from the urea–MPN matrices was complete within 3–9 days, whereas that from pure urea took 1 day (Figure 5b). This finding confirms that urea-encapsulated MPNs can be implemented as a CRU. Specifically, the aged and heated urea–MPN matrices performed better for slow urea release, reaching >90% of urea release by 5 and 7 days, respectively, relative to pure urea (<1 day) and fresh sample (3 days). The slower urea release profile displayed by the heat-treated sample when compared with the aged sample may be attributed to the increase in the coordination interactions among Ti^{IV}–TA complexes from bis- to tris-complexes (Figure 2a). Furthermore, the heated sample exhibited a lag time in the release of urea in the first 3 days. Considering the changes observed in the bulk properties of the urea–MPN matrix after the heat treatment, the lag time in the release of urea may be attributed to the large amount of free space in the sample, where some of the dissolved urea may be confined inside the macropores throughout the urea–MPN matrix, thereby hindering the release of urea. The lag time observed for the heated matrix may also be a result of the higher hydrophobicity of the sample (relative to other samples), as lag periods are generally linked to water infiltration into a material.[14,16,47] Considering the better

performance of the heated matrix, the latter was studied further in subsequent urea release studies.

The content of MPN (10, 20, 40%) in the urea–MPN matrix also influenced the urea release profile. As observed in Figure 5c, the timeframe required to reach complete urea release increased from 3 to 9 days when increasing the MPN content from 10 to 40% in the urea–MPN matrices. The slower release rate observed can be attributed to an increase in the content of –OH and –COOR in MPNs, as the MPN content increases, thereby leading to an increase in interactions with the urea molecules and consequently slower release of urea from the sample. Therefore, all subsequent release studies were performed using urea–MPN matrix with 40% MPN, unless otherwise mentioned.

The effect of the metal ion type on the release profile of urea from the urea–MPN_M matrix was investigated, where M refers to the metal ion (i.e., Fe^{III}, Zn^{II}, Zr^{IV}, or Ti^{IV}) used during synthesis (Figure 5d). The release of urea from urea–MPN_{Ti} or urea@MPN_{Zr} was slower (reaching complete release within ~9 days) than that from urea–MPN_{Zn} or urea–MPN_{Fe}, which achieved complete release within 3 and 5 days, respectively. The slower release rate of urea–MPN_{Ti} and urea–MPN_{Zr} is attributed to both the different coordination bonds between TA and varying metal ions and the higher oxidation state and formal charge of Ti^{IV} and Zr^{IV} (relative to Zn^{II} and Fe^{III}). The latter facilitates the formation of a hydrogel system—which assists with the retention of urea within CRUs and subsequent slower release of urea—following absorption of water by the urea–MPN matrix from soil.[12,13,70–75] Moreover, the heated urea–MPN_{Fe}, used as a model, showed a lower mechanical resistance than heated urea–MPN_{Ti} and urea–MPN_{Zr}, making it less stable in soil and exhibiting a faster urea release rate. It is noted that the metal–phenolic structure can undergo degradation in soil, resulting in the release of metals.[76–78] Zr and Ti are naturally occurring elements that are considered to have low toxicity and are commonly found in soils.[79,80] However, the concentration of Zr or Ti elements used in the urea–

$MPN_{40\%}$ matrices is approximately 1 wt% (equivalent to ~20 mg per kg of soil), which is lower than the concentration at which these elements are naturally present in soil.[79–81]

The environment temperature of the soil also influenced the urea release profiles of urea–MPN_{Ti}. As observed in Figure 5e, elevating the temperature from 10 to 40 °C resulted in shorter urea release profiles, with complete release achieved within 11, 9, and 3 days, respectively. The higher vapor pressure and RH of the urea–MPN_{Ti} matrix in soil system in the container at increased temperatures (i.e., at 40 °C) promote faster water diffusion throughout the sample and consequently an increase in the release rate of urea. In contrast, varying the moisture content of the soil (i.e., 30, 40, and 60% WFPS) had minimal effect on the release profile of urea from the urea–MPN_{Ti} matrix; complete release was achieved within 9 days for all WFPS values studied (Figure 5f). These findings show that vapor pressure has a greater influence than soil moisture on the release rate of urea.

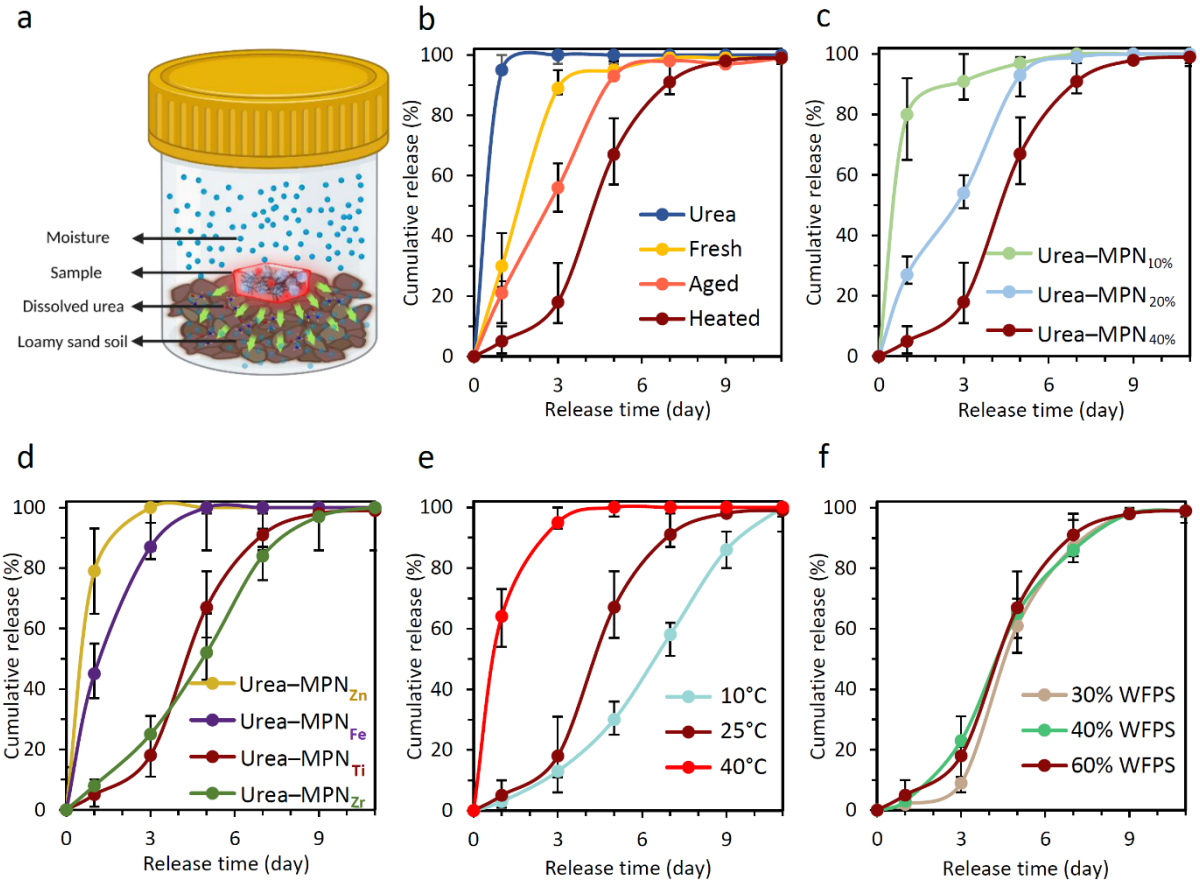

Figure 5. (a) Schematic of the urea release experiment in soil from urea–MPN matrix. (b) Cumulative release rate of urea in soil from urea–MPN matrices subjected to different treatments. MPN content, 40%; metal ion, Ti^{IV}; environmental temperature of soil, 25 °C; soil moisture (WFPS), 60%. (c) Cumulative release rate of urea in soil from heat-treated urea–MPN matrices with varying MPN contents (10, 20, 40%). Metal ion, Ti^{IV}; temperature, 25 °C; WFPS, 60%. (d) Cumulative release rate of urea in soil from heat-treated urea–MPN matrices prepared with different metal ions (Zn^{II}, Fe^{III}, Ti^{IV}, Zr^{IV}). MPN content, 40%; temperature, 25 °C; WFPS, 60%. (e) Cumulative release rate of urea in soil from heat-treated urea–MPN matrix at different environmental temperatures (10, 25, 40 °C). MPN content, 40%; metal ion, Ti^{IV}; WFPS, 60%. (f) Cumulative release rate of urea in soil from heat-treated urea–MPN matrix at varying WFPS (30, 40, 60%). MPN content, 40%; metal ion, Ti^{IV}; temperature, 25 °C. A colorimetric protocol was used for the urea release studies. Three experiments were performed for each sample, and data are shown as the mean ± standard deviation.

Evaluating the nitrogen release profile of CRUs is essential for seedling survival and long-term plant growth. Likewise, the water-holding capacity of soil in the presence of CRUs is an important factor to consider, as this can influence the frequency of irrigation required and/or plant survival in arid and semi-arid areas by creating a water reservoir (via swelling of the materials) near the plant root zone. Thus, the effects of the water-holding capacity of the urea–MPN matrices on the water-holding capacity and water retention of soil were assessed (Figure 6). The water-holding capacity of urea–MPN_{Ti} and urea–MPN_{Zr} with different MPN contents (i.e., 10, 20, 40%) were examined at 25 °C and 70% RH (Figure 6a). The water-holding capacity of the urea–$MPN_{Zr/Ti}$ matrices compared to the dried samples improved from ≈20 to ≈100% w/w by increasing the MPN content in the urea–$MPN_{Zr/Ti}$ matrices, with urea–MPN_{Zr} displaying a slightly higher water-holding capacity than urea–MPN_{Ti}. These results demonstrate the potential of the urea–$MPN_{Zr/Ti}$ matrices as hydrogel CRUs. After

homogeneously mixing the urea–$MPN_{Zr/Ti}$ matrices with 40% MPN content at different levels from 1 to 3% with soil, the water-holding capacity of the soil increased from ≈10 to 25% compared to the control experiment (no added materials), further indicating that the urea–$MPN_{Zr/Ti}$ matrices can be used as a hydrogel system in soil (Figure 6b). In addition, a slower water evaporation rate at 25 °C was observed when 3% of urea–MPN_{Ti} or urea–MPN_{Zr} matrix (with 40% MPN content) was mixed with soil compared to nontreated soil (no added materials), indicating that the water retention of the soil was improved likely due to strong interactions of the urea–$MPN_{Zr/Ti}$ matrices with inorganic and organic matters of the soil (Figure 6c). Therefore, the application of urea–MPN matrix as a hydrogel CRU could be an alternative practice in agriculture to increase the water-holding capacity of soil and improve the synchronicity between nitrogen supply and plant needs by controlling the release of urea. It is noted that the CRU introduced in the present study can be used for vegetable crops[82,83] and is comparable (in terms of the urea release rate) to other controlled-release fertilizers manufactured from hydrophilic biomass compounds.[84,85] Moreover, compared to commercial nonbiodegradable polymer-derived coatings for slow-release fertilizers, the process of developing slow-release fertilizers through mechanochemistry-generated MPNs offers several potential benefits. These include simplified and efficient scalability for continuous production, the elimination of problems linked to solvents, and the introduction of micronutrients into the soil.[34,36,77,86] We are currently further developing the urea–MPN matrices to prolong urea release in extending their suitability for a broader variety of crops.

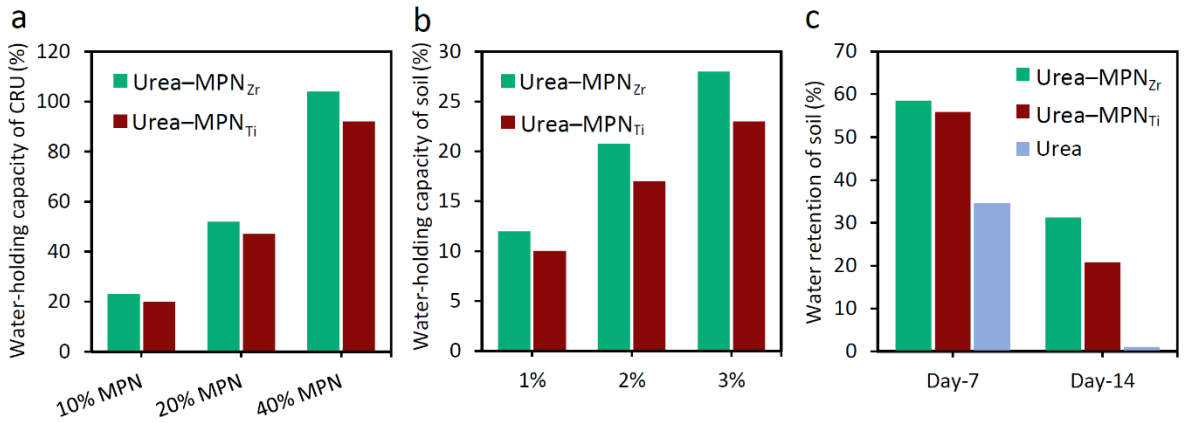

Figure 6. Changes in water-holding capacity and water retention following contact of urea–MPN with water and soil. (a) Water-holding capacity of urea–MPN$_{Zr}$ and urea–MPN$_{Ti}$ matrices prepared using different contents of MPN. (b) Water-holding capacity of soil after the introduction of different contents of urea–MPN$_{Zr}$ or urea–MPN$_{Ti}$ matrix (MPN content, 40%) in soil. (c) Water retention of soil after mixing with urea–MPN$_{Zr}$ or urea–MPN$_{Ti}$ matrix (MPN content 40%). urea–MPN$_{Zr/Ti}$ content in soil = 3%. The experiments were conducted at 25 °C and 70% RH.

CONCLUSION

MPNs were assembled from TA ligands and Ti^{IV} metal ions via a mechanochemistry method. In this process, solid urea was used as an alkaline mediator, resulting in urea-encapsulated MPN matrix (urea–MPN). Subjecting the as-prepared urea–MPN matrix to aging and moderate heating treatment resulted in a shift in the complexation state of the Ti^{IV}–TA coordination from bis to tris-complexes, which influenced the morphology of the resulting material. Heating altered the degree of crystallinity (crystal domain sizes) of the material, leading to changes in the physiochemical properties of the material, including compression resistance, wettability, and stiffness. The in-depth understanding of the mechanochemical synthesis of MPNs mediated by urea and the age-/heat-induced structural rearrangement of MPN and urea crystals within the matrix provide an opportunity to design tunable materials for numerous industrial applications. Urea–MPN matrices prepared from different metals (Zr^{IV}, Ti^{IV}, Zn^{II}, and Fe^{III})

were examined as CRUs. The release of urea could be prolonged for up to 9 days depending on the choice of the metal and treatment applied. This work not only addresses the need for the development of sustainable and scalable CRUs but also examines the implementation of MPNs as a CRU within the agricultural landscape. Further studies are being conducted to examine the hydrogel swelling behavior of these urea–MPN systems, which can further impact the release rate of a range of fertilizers.

ASSOCIATED CONTENT

Supporting Information

The Supporting Information is available free of charge at via the Internet at http://pubs.acs.org. XRD patterns of the fresh, aged, heated urea–MPN matrices, and urea crystals after ball milling; HRTEM image of urea–MPN matrix after aging treatment; DSC curve of urea crystals; WCAs of the surface of fresh, aged, and heated urea–MPN matrices; and compressive stress–strain curve of heated urea–MPN_{Fe} (PDF).

Movie S1. 3D rendering of urea–MPN matrix after aging (MPG).

Movie S2. 3D rendering of urea–MPN matrix after heating (MPG).

AUTHOR INFORMATION

Corresponding Authors

*fcaruso@unimelb.edu.au

*helencs@unimelb.edu.au

*mumfordk@unimelb.edu.au

Author Contributions

The manuscript was written through contributions of all authors. All authors have given approval to the final version of the manuscript.

Notes

The authors declare no competing financial interest.

ACKNOWLEDGMENT

This research was supported under the Australian Research Council (ARC) Industrial Transformation Research Program funding scheme (IH200100023) and the ARC Linkage Project funding scheme (LP160101417). F.C. acknowledges the award of a National Health and Medical Research Council Leadership Fellowship (GNT2016732). A.Z. thanks The University of Melbourne for the support received through the McKenzie Postdoctoral Fellowship Program. The research experiments were partly performed at the Materials Characterization and Fabrication Platform (MCFP) and Bio21 Advanced Microscopy Facility at The University of Melbourne. We thank the Melbourne Trace Analysis for Chemical, Earth, and Environmental Sciences (TrACEES) Platform for access to the micro-CT scanner and Dr. Jay Black (School of Earth Sciences, The University of Melbourne) for technical assistance with the micro-CT analyses. We thank Dr. Roya Khalil from Incitec Pivot Limited for helpful discussions on industrial concepts of the work.

REFERENCES

(1) Free, C. M.; Cabral, R. B.; Froehlich, H. E.; Battista, W.; Ojea, E.; O'Reilly, E.; Palardy, J. E.; García Molinos, J.; Siegel, K. J.; Arnason, R.; et al. Expanding Ocean Food Production under Climate Change. *Nature* **2022**, *605*, 490–496.

(2) Lam, S. K.; Wille, U.; Hu, H.-W.; Caruso, F.; Mumford, K.; Liang, X.; Pan, B.; Malcolm, B.; Roessner, U.; Suter, H.; et al. Next-Generation Enhanced-Efficiency Fertilizers for Sustained Food Security. *Nat. Food* **2022**, *3*, 575–580.

(3) Chen, Q.-L.; Hu, H.-W.; He, Z.-Y.; Cui, L.; Zhu, Y.-G.; He, J.-Z. Potential of Indigenous Crop Microbiomes for Sustainable Agriculture. *Nat. Food* **2021**, *2*, 233–240.

(4) Zhang, X.; Gu, B.; van Grinsven, H.; Lam, S. K.; Liang, X.; Bai, M.; Chen, D. Societal Benefits of Halving Agricultural Ammonia Emissions in China Far Exceed the Abatement Costs. *Nat. Commun.* **2020**, *11*, 4357.

(5) McQuillan, R. V.; Stevens, G. W.; Mumford, K. A. Implementation of Biodegradable Liquid Marbles as a Novel Controlled Release Fertilizer. *ACS Sustainable Chem. Eng.* **2023**, *11*, 122–132.

(6) Jariwala, H.; Santos, R. M.; Lauzon, J. D.; Dutta, A.; Wai Chiang, Y. Controlled Release Fertilizers (CRFs) for Climate-Smart Agriculture Practices: A Comprehensive Review on Release Mechanism, Materials, Methods of Preparation, and Effect on Environmental Parameters. *Environ. Sci. Pollut. Res.* **2022**, *22*, 53967–53995

(7) Pang, L.; Gao, Z.; Feng, H.; Wang, S.; Wang, Q. J. J. o. C. R. Cellulose Based Materials for Controlled Release Formulations of Agrochemicals: A Review of Modifications and Applications. *J. Controlled Release* **2019**, *316*, 105–115.

(8) Azeem, B.; KuShaari, K.; Man, Z. B.; Basit, A.; Thanh, T. H. J. J. o. c. r. Review on Materials & Methods to Produce Controlled Release Coated Urea Fertilizer. *J. Controlled Release* **2014**, *181*, 11–21.

(9) Xie, J.; Yang, Y.; Gao, B.; Wan, Y.; Li, Y. C.; Cheng, D.; Xiao, T.; Li, K.; Fu, Y.; Xu, J.; et al. Magnetic-Sensitive Nanoparticle Self-Assembled Superhydrophobic Biopolymer-

Coated Slow-Release Fertilizer: Fabrication, Enhanced Performance, and Mechanism. *ACS Nano* **2019**, *13*, 3320–3333.

(10) Zhang, S.; Yang, Y.; Tong, Z.; Gao, B.; Gao, N.; Shen, T.; Wan, Y.; Yu, Z.; Liu, L.; Ma, X.; et al. Self-Assembly of Hydrophobic and Self-Healing Bionanocomposite-Coated Controlled-Release Fertilizers. *ACS Appl. Mater. Interfaces* **2020**, *12*, 27598–27606.

(11) Liu, L.; Ni, Y.; Zhi, Y.; Zhao, W.; Pudukudy, M.; Jia, Q.; Shan, S.; Zhang, K.; Li, X. Sustainable and Biodegradable Copolymers from SO_2 and Renewable Eugenol: A Novel Urea Fertilizer Coating Material with Superio Slow Release Performance. *Macromolecules* **2020**, *53*, 936–945.

(12) Mann, M.; Kruger, J. E.; Andari, F.; McErlean, J.; Gascooke, J. R.; Smith, J. A.; Worthington, M. J. H.; McKinley, C. C. C.; Campbell, J. A.; Lewis, D. A.; et al. Sulfur Polymer Composites as Controlled-Release Fertilisers. *Org. Biomol. Chem.* **2019**, *17*, 1929–1936.

(13) Xiang, Y.; Ru, X.; Shi, J.; Song, J.; Zhao, H.; Liu, Y.; Guo, D.; Lu, X. Preparation and Properties of a Novel Semi-IPN Slow-Release Fertilizer with the Function of Water Retention. *J. Agric. Food Chem.* **2017**, *65*, 10851–10858.

(14) Zhang, W.; Xiang, Y.; Fan, H.; Wang, L.; Xie, Y.; Zhao, G.; Liu, Y. Biodegradable Urea–Formaldehyde/PBS and Its Ternary Nanocomposite Prepared by a Novel and Scalable Reactive Extrusion Process for Slow-Release Applications in Agriculture. *J. Agric. Food Chem.* **2020**, *68*, 4595–4606.

(15) Song, J.; Zhao, H.; Zhao, G.; Xiang, Y.; Liu, Y. Novel Semi-IPN Nanocomposites with Functions of Both Nutrient Slow-Release and Water Retention. 1. Microscopic Structure, Water Absorbency, and Degradation Performance. *J. Agric. Food Chem.* **2019**, *67*, 7587–7597.

(16) Ye, H. M.; Li, H.-F.; Wang, C.-S.; Yang, J.; Huang, G.; Meng, X.; Zhou, Q. Degradable Polyester/Urea Inclusion Complex Applied as a Facile and Environment-Friendly Strategy for Slow-Release Fertilizer: Performance and Mechanism. *Chem. Eng. J.* **2020**, *381*, 122704.

(17) Dhiman, A.; Sharma, A. K.; Agrawal, G. Polymer Based Engineered Materials for Sustainable Agriculture. *J. Agric. Sci.* **2022**, *2*, 693–711.

(18) Szczęśniak, B.; Borysiuk, S.; Choma, J.; Jaroniec, M. Mechanochemical Synthesis of Highly Porous Materials. *Mater. Horiz.* **2020**, *7*, 1457–1473.

(19) Wang, G. W. Mechanochemical Organic Synthesis. *Chem. Soc. Rev.* **2013**, *42*, 7668–7700.

(20) Friščić, T.; Halasz, I.; Beldon, P. J.; Belenguer, A. M.; Adams, F.; Kimber, S. A. J.; Honkimäki, V.; Dinnebier, R. E. Real-Time and In Situ Monitoring of Mechanochemical Milling Reactions. *Nat. Chem.* **2013**, *5*, 66–73.

(21) Ayoub, G.; Karadeniz, B.; Howarth, A. J.; Farha, O. K.; Đilović, I.; Germann, L. S.; Dinnebier, R. E.; Užarević, K.; Friščić, T. Rational Synthesis of Mixed-Metal Microporous Metal–Organic Frameworks with Controlled Composition Using Mechanochemistry. *Chem. Mater.* **2019**, *31*, 5494–5501.

(22) Zheng, Q.; Rood, S. L.; Unruh, D. K.; Hutchins, K. M. Unique Supramolecular Complex of Diclofenac: Structural Robustness, Crystal-to-Crystal Solvent Exchange, and Mechanochemical Synthesis. *Chem. Commun.* **2019**, *55*, 7639–7642.

(23) De Bellis, J.; Felderhoff, M.; Schüth, F. Mechanochemical Synthesis of Supported Bimetallic Catalysts. *Chem. Mater.* **2021**, *33*, 2037–2045.

(24) Rainer, D. N.; Morris, R. E. New Avenues for Mechanochemistry in Zeolite Science. *Dalton Trans.* **2021**, *50*, 8995–9009.

(25) Peng, H.; Dong, T.; Yang, S.; Chen, H.; Yang, Z.; Liu, W.; He, C.; Wu, P.; Tian, J.; Peng, Y.; et al. Intra-Crystalline Mesoporous Zeolite Encapsulation-Derived Thermally Robust Metal Nanocatalyst in Deep Oxidation of Light Alkanes. *Nat. Commun.* **2022**, *13*, 295.

(26) Javad Kalbasi, R.; Mansouri, S.; Mazaheri, O. In Situ Polymerization of Poly(vinylimidazole) into the Pores of Hierarchical MFI Zeolite as an Acid–Base Bifunctional Catalyst for One-Pot C–C Bond Cascade Reactions. *Res. Chem. Intermed.* **2018**, *44*, 3279–3291.

(27) Tan, D.; García, F. Main Group Mechanochemistry: From Curiosity to Established Protocols. *Chem. Soc. Rev.* **2019**, *48*, 2274–2292.

(28) Chen, Y.; Mellot, G.; van Luijk, D.; Creton, C.; Sijbesma, R. P. Mechanochemical Tools for Polymer Materials. *Chem. Soc. Rev.* **2021**, *50*, 4100–4140.

(29) Emmerling, S. T.; Germann, L. S.; Julien, P. A.; Moudrakovski, I.; Etter, M.; Friščić, T.; Dinnebier, R. E.; Lotsch, B. V. In Situ Monitoring of Mechanochemical Covalent Organic Framework Formation Reveals Templating Effect of Liquid Additive. *Chem* **2021**, *7*, 1639–1652.

(30) Fiss, B. G.; Richard, A. J.; Douglas, G.; Kojic, M.; Friščić, T.; Moores, A. Mechanochemical Methods for the Transfer of Electrons and Exchange of Ions: Inorganic Reactivity from Nanoparticles to Organometallics. *Chem. Soc. Rev.* **2021**, *50*, 8279–8318.

(31) Yuan, Y.; Wang, T.; Chen, H.; Mahurin, S. M.; Luo, H.; Veith, G. M.; Yang, Z.; Dai, S. Ambient Temperature Graphitization Based on Mechanochemical Synthesis. *Angew. Chem. Int. Ed.* **2020**, *59*, 21935–21939.

(32) Yang, C.; Li, Y.; Chen, Y.; Li, Q.; Wu, L.; Cui, X. Mechanochemical Synthesis of γ-Graphyne with Enhanced Lithium Storage Performance. *Small* **2019**, *15*, 1804710.

(33) Casali, L.; Mazzei, L.; Shemchuk, O.; Sharma, L.; Honer, K.; Grepioni, F.; Ciurli, S.; Braga, D.; Baltrusaitis, J. Novel Dual-Action Plant Fertilizer and Urease Inhibitor: Urea·Catechol Cocrystal. Characterization and Environmental Reactivity. *ACS Sustainable Chem. Eng.* **2019**, *7*, 2852–2859.

(34) Adassooriya, N. M.; Mahanta, S. P.; Thakuria, R. Mechanochemistry as an Emerging Tool for the Preparation of Sustained Release Urea Cocrystals as a Nitrogen Source. *CrystEngComm* **2022**, *24*, 1679–1689.

(35) Bakshi, S.; Banik, C.; Laird, D. A.; Smith, R.; Brown, R. C. Enhancing Biochar as Scaffolding for Slow Release of Nitrogen Fertilizer. *ACS Sustainable Chem. Eng.* **2021**, *9*, 8222–8231.

(36) Zheng, B.; Kabiri, S.; Andelkovic, I. B.; Degryse, F.; da Silva, R.; Baird, R.; Self, P.; McLaughlin, M. J. Mechanochemical Synthesis of Zinc Borate for Use as a Dual-Release B Fertilizer. *ACS Sustainable Chem. Eng.* **2021**, *9*, 15995–16004.

(37) Honer, K.; Pico, C.; Baltrusaitis, J. Reactive Mechanosynthesis of Urea Ionic Cocrystal Fertilizer Materials from Abundant Low Solubility Magnesium- and Calcium-Containing Minerals. *ACS Sustainable Chem. Eng.* **2018**, *6*, 4680–4687.

(38) Kang, J.; Bai, G.; Ma, S.; Liu, X.; Ma, Z.; Guo, X.; Wang, X.; Dai, B.; Zhou, F.; Jia, X. On-Site Surface Coordination Complexation Via Mechanochemistry for Versatile Metal–Phenolic Networks Films. *Adv. Mater. Interfaces* **2019**, *6*, 1801789.

(39) Sun, M.; Guo, H.; Zheng, J.; Wang, Y.; Liu, X.; Li, Q.; Wang, R.; Jia, X. Hydrophobic Octadecylamine-Polyphenol Film Coated Slow Released Urea Via One-Step Spraying Co-Deposition. *Polym. Test.* **2020**, *91*, 106831.

(40) Wang, Y.; Guo, H.; Wang, X.; Ma, Z.; Li, X.; Li, R.; Li, Q.; Wang, R.; Jia, X. Spout Fluidized Bed Assisted Preparation of Poly(tannic acid)-Coated Urea Fertilizer. *ACS Omega* **2020**, *5*, 1127–1133.

(41) Ejima, H.; Richardson, J. J.; Liang, K.; Best, J. P.; van Koeverden, M. P.; Such, G. K.; Cui, J.; Caruso, F. One-Step Assembly of Coordination Complexes for Versatile Film and Particle Engineering. *Science* **2013**, *341*, 154–157.

(42) Xu, W.; Pan, S.; Noble, B. B.; Lin, Z.; Bhangu, S. K.; Kim, C.-J.; Chen, J.; Han, Y.; Yarovsky, I.; Caruso, F. Engineering Flexible Metal-Phenolic Networks with Guest Responsiveness Via Intermolecular Interactions. *Angew. Chem. Int. Ed.* **2023**, *62*, e202302448.

(43) Ju, Y.; Kim, C. J.; Caruso, F. Functional Ligand-Enabled Particle Assembly for Bio–Nano Interactions. *Acc. Chem. Res.* **2023**, *56*, 1826–1837.

(44) Mazaheri, O.; Alivand, M. S.; Zavabeti, A.; Spoljaric, S.; Pan, S.; Chen, D.; Caruso, F.; Suter, H. C.; Mumford, K. A. Assembly of Metal–Phenolic Networks on Water-Soluble Substrates in Nonaqueous Media. *Adv. Funct. Mater.* **2022**, *32*, 2111942.

(45) With, T. K.; Petersen, T. D.; Petersen, B. A Simple Spectrophotometric Method for the Determination of Urea in Blood and Urine. *J. Clin. Pathol.* **1961**, *14*, 202.

(46) Guo, J.; Ping, Y.; Ejima, H.; Alt, K.; Meissner, M.; Richardson, J. J.; Yan, Y.; Peter, K.; von Elverfeldt, D.; Hagemeyer, C. E.; et al. Engineering Multifunctional Capsules through the Assembly of Metal–Phenolic Networks. *Angew. Chem. Int. Ed. Engl.* **2014**, *53*, 5546–5551.

(47) Rahim, M. A.; Björnmalm, M.; Suma, T.; Faria, M.; Ju, Y.; Kempe, K.; Müllner, M.; Ejima, H.; Stickland, A. D.; Caruso, F. Metal–Phenolic Supramolecular Gelation. *Angew. Chem. Int. Ed.* **2016**, *55*, 13803–13807.

(48) Peng, W.-C.; Chen, Y.-C.; He, J.-L.; Ou, S.-L.; Horng, R.-H.; Wuu, D.-S. Tunability of p- and n-Channel Tiox Thin Film Transistors. *Sci. Rep.* **2018**, *8*, 9255.

(49) Rahim, M. A.; Centurion, F.; Han, J.; Abbasi, R.; Mayyas, M.; Sun, J.; Christoe, M. J.; Esrafilzadeh, D.; Allioux, F.-M.; Ghasemian, M. B.; et al. Polyphenol-Induced Adhesive Liquid Metal Inks for Substrate-Independent Direct Pen Writing. *Adv. Funct. Mater.* **2021**, *31*, 2007336.

(50) Reyhani, A.; Mazaheri, O.; Sheikh Alivand, M.; Mumford, K.; Qiao, G. G. Temporal Control of RAFT Polymerization Via Magnetic Catalysis. *Polym. Chem.* **2020**, *11*, 2838–2846.

(51) Espina, A.; Cañamares, M. V.; Jurašeková, Z.; Sanchez-Cortes, S. Analysis of Iron Complexes of Tannic Acid and Other Related Polyphenols as Revealed by Spectroscopic Techniques: Implications in the Identification and Characterization of Iron Gall Inks in Historical Manuscripts. *ACS Omega* **2022**, *7*, 27937–27949.

(52) Tanskanen, A.; Karppinen, M. Iron-Terephthalate Coordination Network Thin Films through In-Situ Atomic/Molecular Layer Deposition. *Sci. Rep.* **2018**, *8*, 8976.

(53) He, Y.; Tang, Y.; Zhang, Y.; MacFarlane, L.; Shang, J.; Shi, H.; Xie, Q.; Zhao, H.; Manners, I.; Guo, J. Driving Forces and Molecular Interactions in the Self-Assembly of Block Copolymers to Form Fiber-Like Micelles. *Appl. Phys. Rev.* **2022**, *9*, 021301.

(54) Fernando, N. L.; Rathnayake, D. T. N.; Kottegoda, N.; Jayanetti, J.; Karunaratne, V.; Jayasundara, D. R. Mechanistic Insights into Interactions at Urea–Hydroxyapatite Nanoparticle Interface. *Langmuir* **2021**, *37*, 6691–6701.

(55) Leng, F.; Robeyns, K.; Leyssens, T. Urea as a Cocrystal Former—Study of 3 Urea Based Pharmaceutical Cocrystals. *Pharmaceutics* **2021**, *13*, 671.

(56) Qiu, X.; Wang, X.; He, Y.; Liang, J.; Liang, K.; Tardy, B. L.; Richardson, J. J.; Hu, M.; Wu, H.; Zhang, Y.; et al. Superstructured Mesocrystals through Multiple Inherent Molecular Interactions for Highly Reversible Sodium Ion Batteries. *Sci. Adv.* **2021**, *7*, eabh3482.

(57) Julien, P. A.; Malvestiti, I.; Friščić, T. The Effect of Milling Frequency on a Mechanochemical Organic Reaction Monitored by In Situ Raman Spectroscopy. *Beilstein J. Org. Chem.* **2017**, *13*, 2160–2168.

(58) Kozawa, T.; Fukuyama, K.; Kushimoto, K.; Ishihara, S.; Kano, J.; Kondo, A.; Naito, M. Effect of Ball Collision Direction on a Wet Mechanochemical Reaction. *Sci. Rep.* **2021**, *11*, 210.

(59) Zhang, P.; Li, H.; Veith, G. M.; Dai, S. Soluble Porous Coordination Polymers by Mechanochemistry: From Metal-Containing Films/Membranes to Active Catalysts for Aerobic Oxidation. *Adv. Mater.* **2015**, *27*, 234–239.

(60) Doumeng, M.; Makhlouf, L.; Berthet, F.; Marsan, O.; Delbé, K.; Denape, J.; Chabert, F. A Comparative Study of the Crystallinity of Polyetheretherketone by Using Density, DSC, XRD, and Raman Spectroscopy Techniques. *Polym. Test.* **2021**, *93*, 106878.

(61) Mazaheri, O.; Kalbasi, R. J. Preparation and Characterization of Ni/mZSM-5 Zeolite with a Hierarchical Pore Structure by Using KIT-6 as Silica Template: An Efficient Bi-Functional Catalyst for the Reduction of Nitro Aromatic Compounds. *RSC Adv.* **2015**, *5*, 34398–34414.

(62) Gross, P.; Höppe, H. A. Biuret—A Crucial Reaction Intermediate for Understanding Urea Pyrolysis to Form Carbon Nitrides: Crystal-Structure Elucidation and In Situ

Diffractometric, Vibrational and Thermal Characterisation. *Chem. Eur. J.* **2020**, *26*, 14366–14376.

(63) Kottegoda, N.; Sandaruwan, C.; Priyadarshana, G.; Siriwardhana, A.; Rathnayake, U. A.; Berugoda Arachchige, D. M.; Kumarasinghe, A. R.; Dahanayake, D.; Karunaratne, V.; Amaratunga, G. A. J. Urea-Hydroxyapatite Nanohybrids for Slow Release of Nitrogen. *ACS Nano* **2017**, *11*, 1214–1221.

(64) Tsuzuki, S.; Orita, H.; Honda, K.; Mikami, M. First-Principles Lattice Energy Calculation of Urea and Hexamine Crystals by a Combination of Periodic DFT and MP2 Two-Body Interaction Energy Calculations. *J. Phys. Chem. B* **2010**, *114*, 6799–6805.

(65) Pereira, E. I.; da Cruz, C. C. T.; Solomon, A.; Le, A.; Cavigelli, M. A.; Ribeiro, C. Novel Slow-Release Nanocomposite Nitrogen Fertilizers: The Impact of Polymers on Nanocomposite Properties and Function. *Ind. Eng. Chem. Res.* **2015**, *54*, 3717–3725.

(66) Javad Kalbasi, R.; Parishani, P.; Mazaheri, O. Encapsulation of Nickel Nanoparticles and Homopoly(vinylsulfonic acid) in Mesoporous Carbon CMK-3 as an Acid–Metal Bifunctional Catalyst for Tandem Reductive Amination. *J. Cluster Sci.* **2018**, *29*, 561–575.

(67) Bhangu, S. K.; Charchar, P.; Noble, B. B.; Kim, C.-J.; Pan, S.; Yarovsky, I.; Cavalieri, F.; Caruso, F. Origins of Structural Elasticity in Metal–Phenolic Networks Probed by Super-Resolution Microscopy and Multiscale Simulations. *ACS Nano* **2022**, *16*, 98–110.

(68) Schmücker, C.; Stevens, G. W.; Mumford, K. A. Liquid Marble Formation and Solvent Vapor Treatment of the Biodegradable Polymers Polylactic Acid and Polycaprolactone. *J. Colloid Interface Sci.* **2018**, *514*, 349–356.

(69) Elhadj, M. S. Y.; Perrin, F. X. Influencing Parameters of Mechanochemical Intercalation of Kaolinite with Urea. *Appl. Clay Sci.* **2021**, *213*, 106250.

(70) Youxin, Z.; Zhen, F.; Yurong, C.; Xianxing, H.; Sheng, Z.; Shuchen, S.; Xiaofei, T. A Bio-Based Hydrogel Derived from Moldy Steamed Bread as Urea-Formaldehyde Loading for Slow-Release and Water-Retention Fertilizers. *ACS Omega* **2021**, *6*, 33462–33469.

(71) Sarmah, D.; Karak, N. Biodegradable Superabsorbent Hydrogel for Water Holding in Soil and Controlled-Release Fertilizer. *J. Appl. Polym. Sci.* **2020**, *137*, 48495.

(72) Saruchi; Kumar, V.; Mittal, H.; Alhassan, S. M. Biodegradable Hydrogels of Tragacanth Gum Polysaccharide to Improve Water Retention Capacity of Soil and Environment-Friendly Controlled Release of Agrochemicals. *Int. J. Biol. Macromol.* **2019**, *132*, 1252–1261.

(73) Liu, L.; Shen, T.; Yang, Y.; Gao, B.; Li, Y. C.; Xie, J.; Tang, Y.; Zhang, S.; Wang, Z.; Chen, J. Bio-Based Large Tablet Controlled-Release Urea: Synthesis, Characterization, and Controlled-Released Mechanisms. *J. Agric. Food Chem.* **2018**, *66*, 11265–11272.

(74) Zhou, T.; Wang, Y.; Huang, S.; Zhao, Y. Synthesis Composite Hydrogels from Inorganic-Organic Hybrids Based on Leftover Rice for Environment-Friendly Controlled-Release Urea Fertilizers. *Sci. Total Environ.* **2018**, *615*, 422–430.

(75) Olad, A.; Zebhi, H.; Salari, D.; Mirmohseni, A.; Reyhani Tabar, A. Water Retention and Slow Release Studies of a Salep-Based Hydrogel Nanocomposite Reinforced with Montmorillonite Clay. *New J. Chem.* **2018**, *42*, 2758–2766.

(76) Guo, J.; Ping, Y.; Ejima, H.; Alt, K.; Meissner, M.; Richardson, J. J.; Yan, Y.; Peter, K.; von Elverfeldt, D.; Hagemeyer, C. E.; et al. Engineering Multifunctional Capsules through the Assembly of Metal–Phenolic Networks. *Angew. Chem. Int. Ed.* **2014**, *53*, 5546–5551.

(77) Wang, Y.; He, Y.; Wang, Q.; Wang, X.; Tardy, B. L.; Richardson, J. J.; Rojas, O. J.; Guo, J. Microporous Membranes for Ultrafast and Energy-Efficient Removal of Antibiotics through Polyphenol-Mediated Nanointerfaces. *Matter* **2023**, *6*, 260–273.

(78) Zand, A. D.; Heir, A. V. Phytoremediation: Data on Effects of Titanium Dioxide Nanoparticles on Phytoremediation of Antimony Polluted Soil. *Data in Brief* **2020**, *31*, 105959.

(79) Lyu, S.; Wei, X.; Chen, J.; Wang, C.; Wang, X.; Pan, D. Titanium as a Beneficial Element for Crop Production. *Front. Plant Sci.* **2017**, *8*, 597.

(80) Shahid, M.; Ferrand, E.; Schreck, E.; Dumat, C. Behavior and Impact of Zirconium in the Soil–Plant System: Plant Uptake and Phytotoxicity. In *Reviews of Environmental Contamination and Toxicology Volume 221*, Whitacre, D. M. Ed.; Springer New York, 2013; pp 107–127.

(81) Cornu, S.; Lucas, Y.; Lebon, E.; Ambrosi, J. P.; Luizão, F.; Rouiller, J.; Bonnay, M.; Neal, C. Evidence of Titanium Mobility in Soil Profiles, Manaus, Central Amazonia. *Geoderma* **1999**, *91*, 281–295.

(82) Hartz, T. K.; Smith, R. F. Controlled-Release Fertilizer for Vegetable Production: The California Experience. *HortTechnology* **2009**, *19*, 20–22.

(83) Sharma, G. C. Controlled-Release Fertilizers and Horticultural Applications. *Sci. Hortic.* **1979**, *11*, 107–129.

(84) Zhang, Y.; Liang, X.; Yang, X.; Liu, H.; Yao, J. An Eco-Friendly Slow-Release Urea Fertilizer Based on Waste Mulberry Branches for Potential Agriculture and Horticulture Applications. *ACS Sustainable Chem. Eng.* **2014**, *2*, 1871–1878.

(85) Iftime, M. M.; Ailiesei, G. L.; Ungureanu, E.; Marin, L. Designing Chitosan Based Eco-Friendly Multifunctional Soil Conditioner Systems with Urea Controlled Release and Water Retention. *Carbohydr. Polym.* **2019**, *223*, 115040.

(86) Rudmin, M.; Abdullayev, E.; Ruban, A.; Buyakov, A.; Soktoev, B. Mechanochemical Preparation of Slow Release Fertilizer Based on Glauconite–Urea Complexes. *Minerals* **2019**, *9,* 507.

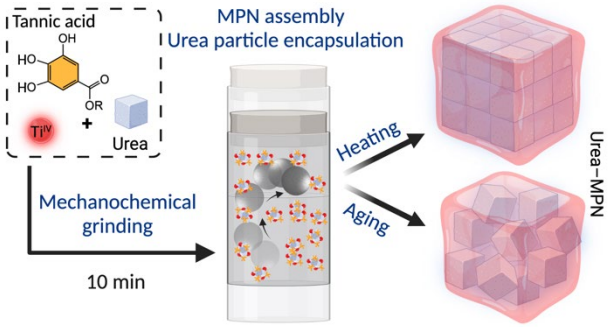
Tannic acid
OH
HO
HO
O
OR
Tiᴵⱽ
+
Urea
Mechanochemical grinding
10 min
MPN assembly
Urea particle encapsulation
Heating
Aging
Urea–MPN